



Performance assessment of a rigid wing Airborne Wind Energy pumping system[☆]

G. Licitra^{a,*}, J. Koenemann^a, A. Bürger^{c,a}, P. Williams^b, R. Ruitenkamp^b, M. Diehl^a

^a Department of Microsystems Engineering, University of Freiburg, Germany

^b Ampyx Power B.V., The Hague, Netherlands

^c Faculty of Management Science and Engineering, Karlsruhe University of Applied Sciences, Germany

ARTICLE INFO

Article history:

Received 3 August 2018

Received in revised form

13 January 2019

Accepted 9 February 2019

Available online 16 February 2019

Keywords:

Airborne Wind Energy

Flight trajectory optimization

Differential algebraic equations

ABSTRACT

This paper presents an Optimal Control Problem (OCP) tailored to assess the system performance of a rigid wing Airborne Wind Energy (AWE) pumping system prior to real flight tests. The proposed method is validated against experimental data obtained using a small prototype designed by the Dutch company Ampyx Power B.V. Within such analysis, it is shown that a non-optimized closed-loop flight control system can generate power to within 10% of the open-loop optimal flight trajectories. Additionally, results demonstrate that the system efficiency does not depend on the trajectory topology, though a significant change in terms of trajectory shape is observed for different wind speeds as a result of trajectory constraints.

© 2019 Published by Elsevier Ltd.

1. Introduction

Wind speed increases significantly with altitude [1]. Conventional wind turbine manufacturers are constantly increasing the size of their systems in order to reach altitudes where the wind sources are abundant. However, such scaling up procedure leads to significant increments in terms of material for both tower structure and foundations, and costs relative to transportation, installation and maintenance. Additionally, it is not possible to arbitrarily increase the size of conventional wind turbines due to physical constraints. As an alternative, the novel Airborne Wind Energy (AWE) technology promises to efficiently capture the wind resources at higher altitudes by replacing the tips of the blades with a tethered airborne airfoil, e. g., a soft kite or a rigid wing.

A wide variety of concepts in the field of AWE can be found in literature [2], although according to Ref. [3] two main branches can

be distinguished. *Drag mode* Airborne Wind Energy Systems (AWESs) generate power using on-board turbines, transmitting power to the ground via a conductive tether. A drag mode AWES is being developed by Makani Power [4].

Lift mode or *Pumping mode* AWESs produce power by performing periodical variation of tether length and tether tension. More precisely, in pumping systems a *production phase* follows a *retraction phase* periodically. During the production phase, the airfoil exerts a high tension on the tether which is anchored to a ground station composed of a winch and an electric generator. The mechanical power is fed to the electric grid after electrical conversion. Due to finite tether length, a retraction phase is required where the tether is wound up by changing the flight pattern and pulling the tether using the winch. In this phase less lifting force is generated, so that significantly less energy needs to be invested in comparison to what has been gained during the *production phase*. An artist's rendering of the two main phases of a pumping mode AWES is shown in Fig. 1 [5].

A pumping mode AWES is being developed by the Dutch company Ampyx Power B.V. [5], but also by other companies such as KPS [6], Twingtec [7], Kitemill [8] and e-kite [9].

Regardless of the system type, the airfoil is required to fly in cyclic patterns to maximize net power produced per cycle, and due to the numerous variables that need to be taken into account simultaneously, the computation of efficient and feasible flight trajectories is not trivial. In many cases, non-optimized flight paths

[☆] This research was supported by the EU via FP7-ITN-TEMPO (607 957) and H2020-ITN-AWESCO (642 682), by the Federal Ministry for Economic Affairs and Energy (BMWi) via eco4wind and DyConPV, by DFG via Research Unit FOR 2401, and by the State Ministry of Baden-Wuerttemberg for Sciences, Research and Arts (Az: 22-7533.-30-20/9/3).

* Corresponding author.

E-mail addresses: gianni.licitra7@gmail.com (G. Licitra), jonas.koenemann@yahoo.de (J. Koenemann), adrian.buenger@hs-karlsruhe.de (A. Bürger), p.williams@ampyxpower.com (P. Williams), r.ruitenkamp@ampyxpower.com (R. Ruitenkamp), moritz.diehl@imtek.uni-freiburg.de (M. Diehl).

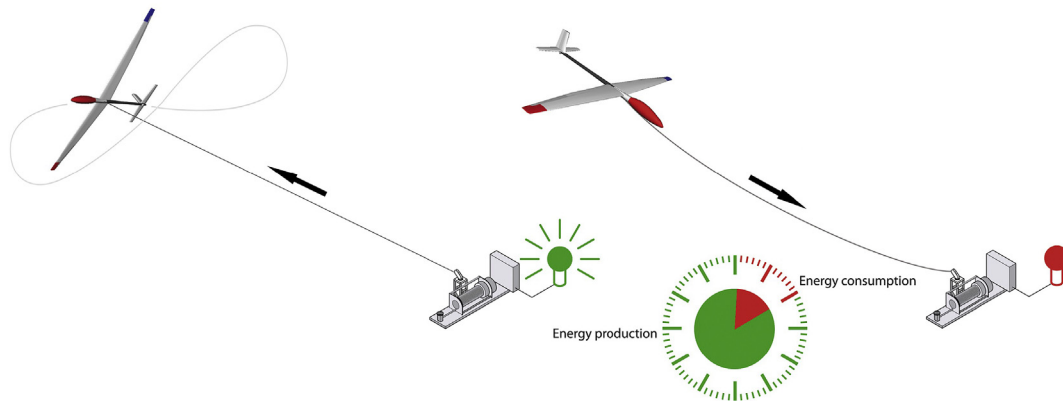


Fig. 1. Working principles of a pumping mode AWES with a production (left) and consumption (right) phase. A lift mode AWES produces power by performing periodical variation of both length and tether tension. Power generation occurs during the so called reel-out phase, where the tether tension is used to rotate a drum, driving an electric generator located on the ground. A reel-in phase is required due to finite tether length. By changing the flight pattern in such a way that less lifting force is produced, the tether can be wound up with a significant lower energy investment than what was gained in the power production phase.

are used as the basis of system sizing and performance prediction, and it is not necessarily obvious how such performance compares with fully optimized trajectories.

In this paper it is shown how to compute optimized flight trajectories and concurrently to assess the system efficiency prior to manufacturing and flight test. The proposed method provides an upper bound of expected performance and it relies on the formulation of an Optimal Control Problem (OCP), where the system dynamics are modeled as a set of Differential Algebraic Equations (DAEs). The OCP is implemented using an open-source tool specifically designed for optimization of AWES. The simulation data are validated via the 2nd prototype designed by Ampyx Power B.V., where the airborne component is a high lift, rigid wing autonomous aircraft (see Fig. 2). Several scenarios are analyzed in terms of control strategy, trajectory topology, and average power output. Finally, the power curve of the case study is carried out and its harvesting factor is analyzed.

The paper is organized as follows. Section 1 introduces the mathematical model of a rigid wing pumping mode AWES suitable for use within OCPs. First, an introduction of the reference frames, wind profile and aircraft characteristics are provided. Subsequently,

each system component is modeled separately via Newtonian mechanics. The system dynamics are ultimately formulated as a set of DAEs. Section 2 formulates an OCP that aims towards the optimization of flight trajectories to maximize the average power output. The optimization tool is validated against a set of experimental data in Section 2.7. Within such analysis, the discrepancy between an optimal open-loop solution with a simulated closed-loop solution carried out using the actual Flight Control Computer (FCC) designed by Ampyx Power B.V. is quantified. In Section 3.1, the lemniscate trajectory is compared to a circular trajectory under equal boundary conditions in terms of power output and size. Finally, in Section 3.2, the power curve and harvesting factor are computed for the case study by solving a sequence of optimal control problems for a range of wind speeds.

2. Modeling of a rigid wing AWES

This section proposes a mathematical formulation of a rigid wing AWE pumping system tailored to OCPs. First, the wind shear is described analytically by a standard power law. Subsequently, a brief introduction to both aircraft attitude and reference frames is



Fig. 2. The 2nd prototype high lift, rigid wing autonomous aircraft designed by Ampyx Power B.V [5], and build in 2009.

provided. Each system component is modeled separately via Newtonian mechanics. Finally, the overall system dynamics are described as a set of DAEs.

2.1. Wind profile modeling

For trajectory optimization of AWES via OCPs, the wind field is normally modeled via a vertical profile of wind speed with no stochastic phenomena such as turbulence fluctuations and low level jets [10]. One of the most common wind profile models approximates the wind speed w as a function of the altitude h by a power law as follows [1]:

$$w(h) = w_{h_a} \left(\frac{h}{h_a} \right)^{c_f} \quad (1)$$

with h_a the anemometer height at which the wind speed w_{h_a} is measured, where c_f denotes the power law exponent that accounts for the effects of obstacles protruding from the earth's surface. High obstacles involve high values of c_f and vice-versa. Typical values of c_f are listed in Table 1, though one may also obtain wind shear characteristics from experimental data for a specific location. For the presented case study, a coefficient of $c_f = 0.15$ is chosen [5].

2.2. Reference frames and aircraft attitude

In order to describe any motion or position, one needs one or more reference frames. For an AWES composed of a rigid wing aircraft, it is convenient to adopt reference frame conventions commonly used in the aerospace field. Under the assumption of a flat earth, let us define a non inertial, right handed orthogonal axis system, where the x and y axis point to the northern and eastern axis, respectively, while the z -axis points downward, toward the Earth's surface. Such frame is known as North-East-Down (NED) frame \mathbf{n} where $\mathbf{p}^{\mathbf{n}} = [p_N, p_E, p_D]^T$ denotes the NED coordinates relative to the aircraft motion with $\mathbf{v}^{\mathbf{n}} = [v_N, v_E, v_D]^T$ the corresponding velocity vector. Likewise, let us consider a body reference frame \mathbf{b} where $\mathbf{e}_x, \mathbf{e}_y, \mathbf{e}_z$ denote the aircraft longitudinal, transversal and vertical axis.

Any vector can be converted into a specific frame by means of Direction Cosine Matrices (DCMs), known also as rotation (transformation) matrices. Within this framework, let us denote $\mathbf{R}_{\mathbf{bn}} \in \mathbb{R}^{3 \times 3}$ as the DCM from NED to body frame. By definition, the inverse transformation of $\mathbf{R}_{\mathbf{bn}}$, i. e., $\mathbf{R}_{\mathbf{nb}}$ (from body to NED frame) is simply given by

$$\mathbf{R}_{\mathbf{nb}} = \mathbf{R}_{\mathbf{bn}}^{-1} = \mathbf{R}_{\mathbf{bn}}^T \quad (2)$$

where the *orthonormality condition* $\Xi_c(\mathbf{R}_{\mathbf{nb}})$ given as

$$\Xi_c(\mathbf{R}_{\mathbf{nb}}) = \mathbf{R}_{\mathbf{nb}} \cdot \mathbf{R}_{\mathbf{nb}}^T - \mathbf{I}_3 \quad (3)$$

must always be equal to zero.

In flight dynamics, one can define the time evolution of $\mathbf{R}_{\mathbf{nb}}$ as [11,12].

Table 1
Friction coefficient c_f for various terrain types [42].

Terrain characteristics	$c_f[-]$
Smooth hard ground, calm water	0.10
Tall grass on level ground	0.15
High crops, hedges and shrubs	0.20
Small town with trees and shrubs	0.30
Large city with tall buildings	0.40

$$\dot{\mathbf{R}}_{\mathbf{nb}} = \mathbf{R}_{\mathbf{nb}} \cdot \boldsymbol{\Omega} \quad (4)$$

where $\boldsymbol{\Omega}$ denotes the skew-symmetric matrix of the aircraft angular body rates $\boldsymbol{\omega}^{\mathbf{b}} = [p, q, r]^T$ and defined as

$$\boldsymbol{\Omega} = \begin{bmatrix} 0 & -r & q \\ r & 0 & -p \\ -q & p & 0 \end{bmatrix}. \quad (5)$$

Note that $\mathbf{R}_{\mathbf{nb}}$ embeds the unit vectors which describe the aircraft attitude, i. e.,

$$\mathbf{R}_{\mathbf{nb}} = [\mathbf{e}_x \ \mathbf{e}_y \ \mathbf{e}_z]. \quad (6)$$

Finally, it is possible to extract the angle of roll ϕ , pitch θ and yaw ψ using the ij entries of $\mathbf{R}_{\mathbf{nb}}$ by Ref. [13].

$$\phi = \arctan(r_{32}/r_{33}) \quad \phi \in (-\pi, \pi) \quad (7a)$$

$$\theta = -\arcsin(-r_{31}) \quad \theta \in (-\pi/2, \pi/2) \quad (7b)$$

$$\psi = \arctan(r_{21}/r_{11}) \quad \psi \in (-\pi, \pi), \quad (7c)$$

and as a result the aircraft attitude can be eventually bounded within an OCP framework via the Euler angles.

2.3. Airframe and physical characteristics

The presented AWES deploys as airborne component a high lift, rigid wing, single fuselage, autonomous aircraft. The airframe is equipped with aileron δ_a , elevator δ_e and rudder δ_r , entirely actuated via electric servos. The aircraft is also equipped with flaps and propulsion system, though, they are not exploited during cross-wind flights.

The airframe geometry, i. e., wing span b , aerodynamic chord \bar{c} , wing area S , aspect ratio AR are collected in Table 2 as well as the mass m and moments of inertia J_i with $i = x, y, z, xz$ relative to the body axes, and due to symmetry along longitudinal axis, the aircraft yields an inertia matrix \mathbf{J} equal to

$$\mathbf{J} = \begin{bmatrix} J_x & 0 & -J_{xz} \\ 0 & J_y & 0 \\ -J_{xz} & 0 & J_z \end{bmatrix}. \quad (8)$$

2.4. Rigid body equations

The mathematical model of a high lift, rigid wing tethered aircraft can be obtained using the six degree of freedom Equation of Motion (EOM) as for modeling a conventional aircraft, i. e.,

Table 2
Physical properties of the aircraft designed by Ampyx Power B.V [5].

Name	Symbol	Value	Unit
Mass	m	36.8	[kg]
Moment of inertia	J_x	25	[kg·m ²]
Moment of inertia	J_y	32	[kg·m ²]
Moment of inertia	J_z	56	[kg·m ²]
Cross moment of inertia	J_{xz}	0.47	[kg·m ²]
Reference wing span	b	5.5	[m]
Reference chord	\bar{c}	0.55	[m]
Reference wing area	S	3	[m ²]
Aspect ratio	AR	10	[-]

$$\mathbf{m} \cdot \dot{\mathbf{v}}^b = \mathbf{f}_t^b + \mathbf{f}_a^b + \mathbf{f}_g^b - m (\boldsymbol{\omega}^b \times \mathbf{v}^b) \quad (9a)$$

$$\mathbf{J} \cdot \dot{\boldsymbol{\omega}}^b = \mathbf{m}_a^b - (\boldsymbol{\omega}^b \times \mathbf{J} \cdot \boldsymbol{\omega}^b) \quad (9b)$$

where (9a) is the translational acceleration and (9b) the angular momentum, both expressed in body frame. Assuming the airframe as a rigid body, the aircraft is subject to forces coming from the tether $\mathbf{f}_t^b = [X_t, Y_t, Z_t]^T$, aerodynamic characteristics $\mathbf{f}_a^b = [X, Y, Z]^T$ and gravity \mathbf{f}_g^b . Normally, the tether attachment point is located close to the aircraft center of gravity, hence, one can neglect the moments caused by the tether and consider only the aerodynamic contribution $\mathbf{m}_a^b = [l, m, n]^T$. The gravitational force defined in body frame is simply equal to

$$\mathbf{f}_g^b = \mathbf{R}_{bn} \begin{bmatrix} 0 \\ 0 \\ g_D \end{bmatrix} = mg_D \begin{bmatrix} -\sin \theta \\ \cos \theta \sin \phi \\ \cos \theta \cos \phi \end{bmatrix} \quad (10)$$

with $g_D \approx 9.81 \text{ m/s}^2$. As far as it regards the aerodynamic characteristics ($\mathbf{f}_a^b, \mathbf{m}_a^b$), they are generated by the aircraft relative motion with respect to the air mass, i. e.,

$$\mathbf{v}_r^b = \mathbf{v}^b - \mathbf{R}_{bn} \mathbf{v}_w^n = [v_{r_x}^b, v_{r_y}^b, v_{r_z}^b]^T \quad (11)$$

with \mathbf{v}_r^b the relative velocity expressed in body frame and \mathbf{v}_w^n the local wind velocity vector defined in NED frame. Throughout this work, the wind direction points North, i. e.,

$$\mathbf{v}_w^n = [w(h), 0, 0]^T \quad (12)$$

with $w(h)$ shown in (1). Additionally, aerodynamic properties depend on the orientation of the aircraft w.r.t. the airflow. Such effect is modeled via the so called *aerodynamic states* which are given by Ref. [13].

$$V_T = \|\mathbf{v}_r^b\|_2 \quad (13a)$$

$$\beta = \arcsin(v_{r_y}^b / V_T) \quad (13b)$$

$$\alpha = \arctan(v_{r_z}^b / v_{r_x}^b) \quad (13c)$$

with V_T the true airspeed, β the angle of side-slip and α the angle of attack. The nomenclature introduced above is summarized in Fig. 3.

One can also define the translational acceleration (9a) in NED frame by

$$\mathbf{m} \cdot \dot{\mathbf{v}}^n = \mathbf{R}_{nb} \cdot (\mathbf{f}_t^b + \mathbf{f}_a^b + \mathbf{f}_g^b). \quad (14)$$

Finally, for optimal control purposes it is convenient to take into account the servo speed which mathematically read as

$$\dot{\boldsymbol{\delta}} = \mathbf{v}_\delta \quad (15)$$

with $\boldsymbol{\delta} = [\delta_a, \delta_e, \delta_r]^T$ the control surface deflections and $\mathbf{v}_\delta = [v_{\delta_a}, v_{\delta_e}, v_{\delta_r}]^T$ the corresponding actuator speed vector.

2.5. Aerodynamic forces and moments

The aerodynamic properties ($\mathbf{f}_a^b, \mathbf{m}_a^b$) are defined in the body frame and normalized with respect to the dynamic pressure $\bar{q} = \frac{1}{2} \rho V_T^2$ with $\rho \approx 1.225 \text{ kg/m}^3$ the free-stream mass density, and a characteristic area of the aircraft body as follows [13].

$$X = \bar{q} S C_X : \text{Axial Force} \quad (16a)$$

$$Y = \bar{q} S C_Y : \text{Side Force} \quad (16b)$$

$$Z = \bar{q} S C_Z : \text{Vertical Force} \quad (16c)$$

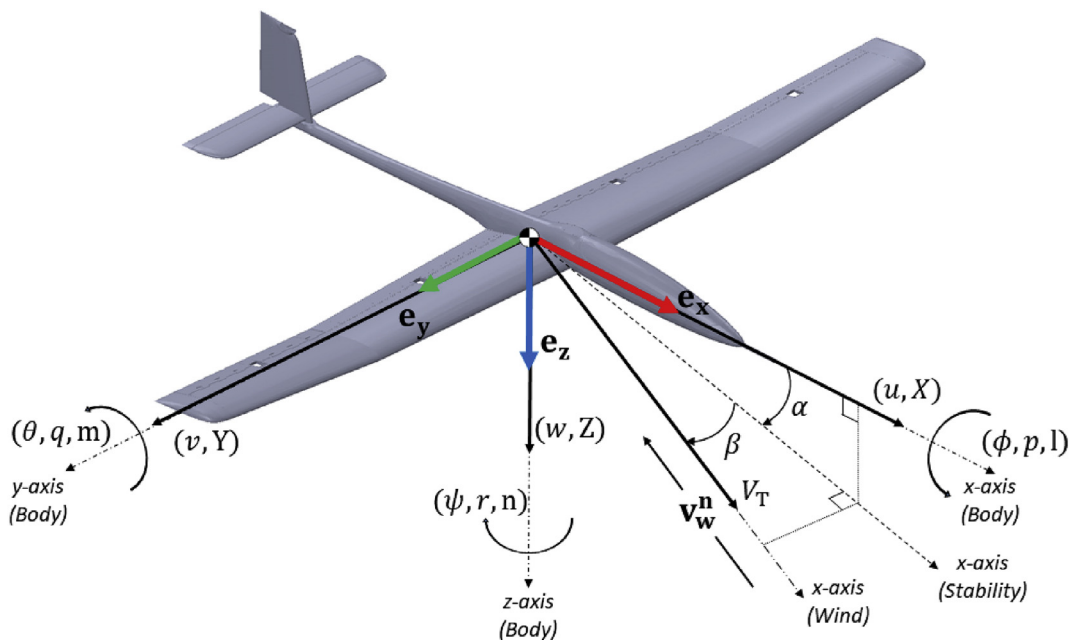


Fig. 3. Definition of axes, body angular rates and velocity, Euler angles, aerodynamic states, forces and moments of an aircraft.

$$l = \bar{q} S b C_l : \text{Rolling Moment} \quad (16d)$$

$$m = \bar{q} S c C_m : \text{Pitching Moment} \quad (16e)$$

$$n = \bar{q} S b C_n : \text{Yawing Moment} \quad (16f)$$

where C_X, C_Y, C_Z and C_l, C_m, C_n are the *non-dimensional body-axes aerodynamic force and moment coefficients*, respectively. In the aerodynamic field, it is common practice to approximate the aerodynamic coefficients by linear terms in their Taylor series expansion as follows [11].

$$C_X = C_{X_\alpha} \alpha + C_{X_q} \hat{q} + C_{X_{\delta_e}} \delta_e + C_{X_0}, \quad (17a)$$

$$C_Y = C_{Y_\beta} \beta + C_{Y_p} \hat{p} + C_{Y_r} \hat{r} + C_{Y_{\delta_a}} \delta_a + C_{Y_{\delta_e}} \delta_e, \quad (17b)$$

$$C_Z = C_{Z_\alpha} \alpha + C_{Z_q} \hat{q} + C_{Z_{\delta_e}} \delta_e + C_{Z_0}, \quad (17c)$$

$$C_l = C_{l_\beta} \beta + C_{l_p} \hat{p} + C_{l_r} \hat{r} + C_{l_{\delta_a}} \delta_a + C_{l_{\delta_e}} \delta_e, \quad (17d)$$

$$C_m = C_{m_\alpha} \alpha + C_{m_q} \hat{q} + C_{m_{\delta_e}} \delta_e + C_{m_0}, \quad (17e)$$

$$C_n = C_{n_\beta} \beta + C_{n_p} \hat{p} + C_{n_r} \hat{r} + C_{n_{\delta_a}} \delta_a + C_{n_{\delta_e}} \delta_e, \quad (17f)$$

which depend on the normalized body rates $\hat{p} = \frac{b p}{2V_T}$, $\hat{q} = \frac{\bar{c} q}{2V_T}$, $\hat{r} = \frac{b r}{2V_T}$, angle of attack α and side slip β , as well as the control surface deflections δ . The coefficients C_{ij} with $i = \{X, Y, Z, l, m, n\}$ and $j = \{\alpha, \beta, p, q, r, \delta_a, \delta_e, \delta_e, 0\}$ denote the *dimensionless aerodynamic derivatives* and for this application they are implicitly functions of the angle of attack α .

Aerodynamic derivatives are usually stored as parameters in the form of 1-D look-up tables as for this application. Within this work, 1-D look-up tables are interpolated using polynomial functions of order up to second degree, i. e., $p(\alpha) = c_2 \cdot \alpha^2 + c_1 \cdot \alpha + c_0$, where the polynomial coefficients (c_0, c_1, c_2) are collected in Table 3 and Table 4.

2.6. Tether modeling

The main difference between a conventional aircraft and an aircraft deployed in an AWES is the presence of a tether which

Table 3
Polynomial coefficients relative to C_X, C_Y and C_Z .

C_X	c_0	c_1	C_Y	c_0	c_1	C_Z	c_0	c_1	c_2
C_{X_α}	-	8.320	C_{Y_β}	-0.186	-	C_{Z_α}	-	1.226	10.203
C_{X_q}	-0.603	4.412	C_{Y_p}	-0.102	-	C_{Z_q}	-7.556	0.125	6.149
$C_{X_{\delta_e}}$	-0.011	0.112	C_{Y_r}	0.169	0.137	$C_{Z_{\delta_e}}$	-0.315	-0.001	0.292
C_{X_0}	0.456	-	$C_{Y_{\delta_a}}$	-0.050	-	C_{Z_0}	-5.400	-	-
-	-	-	$C_{Y_{\delta_e}}$	0.103	-	-	-	-	-

Table 4
Polynomial coefficients relative to C_l, C_m and C_n .

C_l	c_0	c_1	C_m	c_0	c_1	C_n	c_0	c_1
C_{l_β}	-0.062	-	C_{m_α}	-	0.205	C_{n_β}	0.058	-0.085
C_{l_p}	-0.559	-	C_{m_q}	-11.302	-0.003	5.289	C_{n_p}	-0.057
C_{l_r}	0.181	0.645	$C_{m_{\delta_e}}$	-1.019	-	-	C_{n_r}	-0.052
$C_{l_{\delta_a}}$	-0.248	0.041	C_{m_0}	-0.315	-	-	$C_{n_{\delta_a}}$	0.019
$C_{l_{\delta_e}}$	0.004	-	-	-	-	-	$C_{n_{\delta_e}}$	-0.041

induces additional forces, moments (if the tether is not placed at the Center of Gravity (CG) of the aircraft) and weight. An accurate tether modeling that takes into account, e.g., aeroelastic effects and tether sag, would significantly increase the overall model complexity (details in Refs. [14–16]), though, if one models the tether as a rigid link, then it is possible to obtain a mathematical formulation that is computationally attractive as shown in Refs. [10,12,17,18].

Within this work, the tether force expressed in body frame \mathbf{f}_t^b is the summation of three contributions, i. e.,

$$\mathbf{f}_t^b = \mathbf{f}_{t_\lambda}^b + \mathbf{f}_{t_g}^b + \mathbf{f}_{t_a}^b \quad (18)$$

with $\mathbf{f}_{t_\lambda}^b$, $\mathbf{f}_{t_g}^b$ and $\mathbf{f}_{t_a}^b$ the vectors of tension, weight and aerodynamic forces relative to the tether, respectively. The tension vector $\mathbf{f}_{t_\lambda}^b$ is first obtained in NED frame and subsequently converted to body frame as follows

$$\mathbf{f}_{t_\lambda}^b = \mathbf{R}_{bn} \mathbf{f}_{t_\lambda}^n \quad (19)$$

where $\mathbf{f}_{t_\lambda}^n$ is introduced in Section 1.8, whereas $\mathbf{f}_{t_g}^b$ is given by

$$\mathbf{f}_{t_g}^b = \mathbf{R}_{bn} (\hat{\mathbf{e}}_z \rho_t g_D l) \quad (20)$$

with $l = \sqrt{p_N^2 + p_E^2 + p_D^2}$ the tether length, ρ_t its linear density, and $\hat{\mathbf{e}}_z = [0, 0, 1]^T$.

Finally, the aerodynamic tether force $\mathbf{f}_{t_a}^b$ is obtained assuming the tether velocity as a linear function of both length l and aircraft speed V_T , and for small side slip angles β , $\mathbf{f}_{t_a}^b$ can be expressed as

$$\mathbf{f}_{t_a}^b = -D_t \begin{bmatrix} \cos \alpha \\ 0 \\ \sin \alpha \end{bmatrix} \quad (21)$$

with D_t the equivalent drag force on the aircraft defined as [19–21].

$$D_t = \left(\frac{d_t C_{D_t}}{4} \right) \bar{q} l. \quad (22)$$

Note that such an approximation implicitly neglects crosswind tether forces and it assumes low wind conditions. As a consequence, the model prediction with the underlying assumption shown in (21) will predict an underestimation of the tether drag for high wind conditions [22,23]. Table 5 collects the tether characteristics relative to the case study.

2.7. Ground station modeling

The ground station is basically composed of a winch mechanism connected to an electric motor as shown in Fig. 4. The mechanical components can be modeled via the energy variation E , i. e.,

$$\dot{E} = \mathbf{f}_{t_\lambda} \omega_d r_d \quad (23)$$

with r_d the drum radius, and ω_d the winch rotational speed. Note that, \dot{E} is equivalent to the mechanical instantaneous power P_m .

As already mentioned, during the power generation (reel-out)

Table 5
Physical properties of the tether.

Name	Symbol	Value	Unit
Drag coefficient	C_{D_t}	1.2	[-]
Linear density	ρ_t	0.0046	[kg/m]
Diameter	d_t	0.002	[kg]

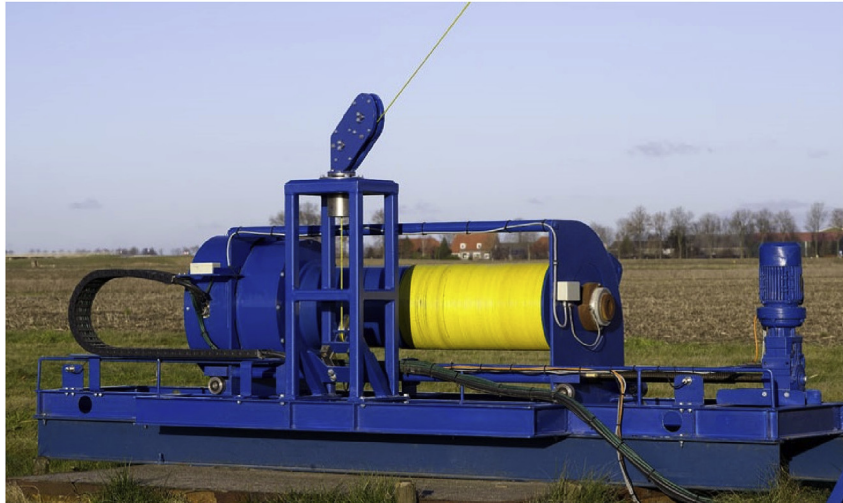


Fig. 4. The ground station converts the mechanical energy from tether tension into electrical power and feeds it to the grid.

phase the tether tension is used to rotate the drum so as to generate electricity. Subsequently, a reset (reel-in) phase is required in order to wind the tether up to its initial condition. As a consequence, the working principles of a lift mode AWES is characterized by periodical variations of the tether length that can be modeled as

$$\dot{l} = v_l \tag{24a}$$

$$\dot{v}_l = a_l \tag{24b}$$

where v_l denotes the tether speed and a_l the corresponding acceleration. Within this work, only the mechanical power P_m is taken into account since experimental data coming from the flight tests do not include measurements of electrical power.

2.8. Modeling of AWESs via DAEs

In summary, a rigid wing pumping mode AWES is characterized by a high lift rigid wing autonomous aircraft connected to a winch located on the ground via a tether. As mentioned in Section 1.6, the tether is assumed as a rigid link with mass and drag. As a consequence, the corresponding tether force $\mathbf{f}_{t_i}^n$ in NED frame and tether tension f_{t_i} can simply be defined as a function of a scalar variable λ as follows:

$$\mathbf{f}_{t_i}^n = -\lambda \mathbf{p}^n \tag{25a}$$

$$f_{t_i} = \lambda \|\mathbf{p}^n\|_2 = \lambda l. \tag{25b}$$

If the ground station is located at the origin of a right-handed Cartesian coordinate system as shown in Fig. 5, then λ must be

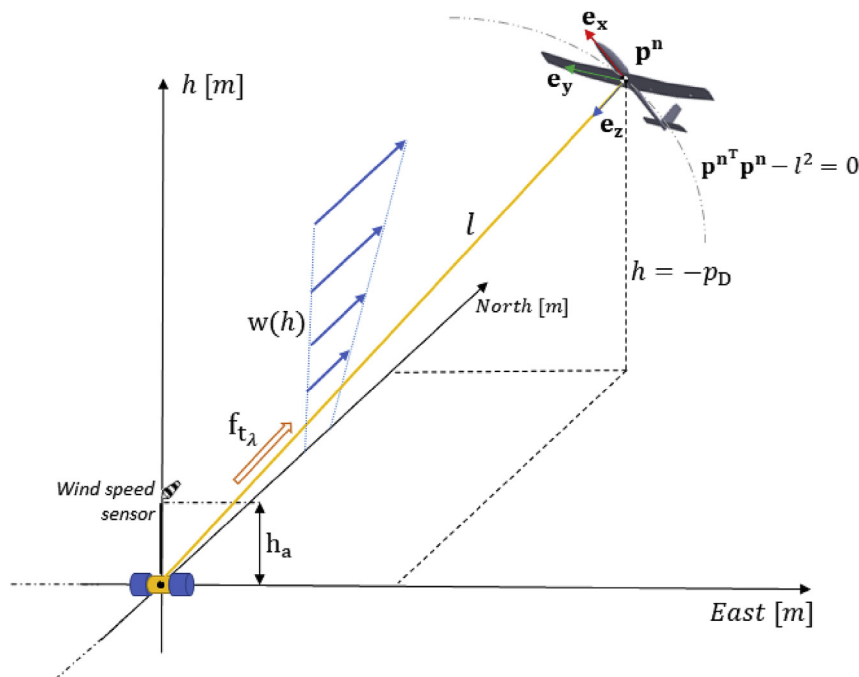


Fig. 5. Graphical representation of a rigid wing pumping mode AWES. The ground station is located at the origin of a right-handed Cartesian coordinate system. Within this work the wind direction points North.

chosen such that the aircraft dynamics evolve in the manifold described by the consistency condition equal to Ref. [12].

$$c(\mathbf{p}^n, l) = \mathbf{p}^{n\top} \mathbf{p}^n - l^2 = 0. \quad (26)$$

Therefore, an AWES can be described by a set of ODEs which are subject to the consistency conditions (26). Additionally, if the aircraft attitude is described via the time evolution of \mathbf{R}_{nb} as in (4), then the orthonormality condition $\Xi_c(\mathbf{R}_{nb})$ (3) must be considered.

Ultimately, the mathematical model of a pumping mode AWES suitable for optimal control purposes takes into account a set of ODEs equal to Ref. [10]:

$$\dot{\mathbf{p}}^n = \mathbf{v}^n \quad (27a)$$

$$\mathbf{m} \cdot \dot{\mathbf{v}}^n = \mathbf{R}_{nb} \cdot (\mathbf{f}_{t_x}^b + \mathbf{f}_{t_y}^b + \mathbf{f}_{t_z}^b + \mathbf{f}_a^b + \mathbf{f}_g^b) \quad (27b)$$

$$\dot{\mathbf{R}}_{nb} = \mathbf{R}_{nb} \cdot \boldsymbol{\Omega} \quad (27c)$$

$$\mathbf{J} \cdot \dot{\boldsymbol{\omega}}^b = \mathbf{m}_a^b - (\boldsymbol{\omega}^b \times \mathbf{J} \cdot \boldsymbol{\omega}^b) \quad (27d)$$

$$\dot{\delta} = \mathbf{v}_\delta \quad (27e)$$

$$\dot{l} = v_l \quad (27f)$$

$$\dot{v}_l = a_l \quad (27g)$$

$$\dot{E} = \mathbf{f}_{t_x} \Gamma_d \omega_d \quad (27h)$$

and a set of algebraic equations which correspond to the following consistency constrains:

$$0 = \mathbf{R}_{nb} \cdot \mathbf{R}_{nb}^\top - \mathbf{I}_3 \quad (28a)$$

$$0 = \mathbf{p}^{n\top} \mathbf{p}^n - l^2 \quad (28b)$$

with differential states $\mathbf{x} = [\mathbf{p}^n, \mathbf{v}^n, \mathbf{R}_{nb}, \boldsymbol{\omega}^b, \delta, l, v_l, E]^\top \in \mathbf{R}^{24}$, control inputs, $\mathbf{u} = [v_{\delta_x}, v_{\delta_y}, v_{\delta_z}, a_l]^\top \in \mathbf{R}^4$ and algebraic variable $\mathbf{z} = \lambda \in \mathbf{R}$.

The model implicitly takes into account the physical characteristics of each subsystem as well as the aerodynamic properties described in Section 1.5. Due to the algebraic equations, the system dynamics are therefore described by a set of DAEs. In Ref. [12], it is shown that a pumping mode AWES modeled via natural coordinates (as in this case) delivers an index-3 DAE which can be subsequently converted into an index-1 DAE to allow the implementation of classical integration methods within an OCP framework (for further details, refer to Ref. [24]).

3. Formulation of an OCP for AWES

In this section, a brief introduction to continuous time OCPs subject to DAEs is provided. Subsequently, an OCP for maximum average power output is formulated for the case study. Finally, the optimal solution is compared and validated against real flight test experiments.

3.1. Overview of continuous time OCPs

In an DAE setting, a continuous time OCP can be stated as follows [25].

$$\underset{\mathbf{x}(\cdot), \mathbf{z}(\cdot), \mathbf{u}(\cdot)}{\text{minimize}} \int_0^T L(\mathbf{x}(t), \mathbf{z}(t), \mathbf{u}(t)) dt + M(\mathbf{x}(T), \mathbf{z}(T)) \quad (29a)$$

$$\text{subject to } \mathbf{F}(\dot{\mathbf{x}}(t), \mathbf{x}(t), \mathbf{z}(t), \mathbf{u}(t)) = \mathbf{0}, \quad t \in [0, T] \quad (29b)$$

$$\mathbf{h}(\dot{\mathbf{x}}(t), \mathbf{x}(t), \mathbf{z}(t), \mathbf{u}(t)) \leq \mathbf{0}, \quad t \in [0, T] \quad (29c)$$

$$\mathbf{r}(\mathbf{x}(0), \mathbf{x}(T)) = \mathbf{0} \quad (29d)$$

with T the observation time, $L(\cdot)$ the integrand (*Lagrange*) term and $M(\cdot)$ the terminal (*Mayer*) cost term. The OCP (29) is subject to a system described by a set of fully-implicit Differential Algebraic Equations DAEs (29b), *path constraints* (29c) which bound the system dynamics in agreement with, e. g., physical limitations, whereas the *boundary constraints* (29d) embrace either fixed initial values or periodic conditions as well as consistency constraints associated to the DAE formulation.

3.2. Characterization of cost function

The main goal of an AWES is to maximize the average power output using an efficient control strategy, while simultaneously delivering feasible flight trajectories in agreement with the system characteristics. By definition, the mechanical average power P_{AV} over a trajectory can be written as

$$P_{AV} = \frac{1}{T} \int_0^T P_m(t) dt \quad (30)$$

where in this case the instantaneous mechanical power $P_m(t)$ can be expressed either using the rotational or translational variables, i. e.,

$$P(t) = \dot{E}(t) = \mathbf{f}_{t_x}(t) \cdot \mathbf{v}_l(t) = \mathbf{m}_{t_x}(t) \cdot \boldsymbol{\omega}_d(t). \quad (31)$$

If one assumes that for $t = 0$ the harvested energy E is equal to 0, then P_{AV} can be expressed as a Mayer cost term within the OCP (29) as follows:

$$P_{AV} = M(\mathbf{x}(T), \mathbf{z}(T)) = \frac{E(T)}{T}. \quad (32)$$

In other words, the mechanical average power can be defined as a function of the harvested energy evaluated at the final time T .

Beyond the maximization of the system performance, well designed flight trajectories should preferably avoid aggressive maneuvers, high accelerations that may provide unacceptable mechanical stress on the aircraft, tether damage as well as significant side forces caused by high side slip angles. For these reasons, the Lagrange cost term is formulated as follows

$$L(\mathbf{x}(t), \mathbf{u}(t)) = \mathbf{u}(t)_{\Sigma_u^{-1}}^2 + \dot{\boldsymbol{\omega}}^b(t)_{\Sigma_\omega^{-1}}^2 + \sigma_\beta^{-1} \beta^2(t) \quad (33)$$

with $\Sigma_u^{-1} \in \mathbf{R}^{4 \times 4}$, $\Sigma_\omega^{-1} \in \mathbf{R}^{3 \times 3}$, $\sigma_\beta^{-1} \in \mathbf{R}$ the weighting matrices associated to the control inputs, aircraft angular accelerations and side slip angle, respectively. Finally, one also aims to harvest the maximum amount of energy within the shortest but feasible time in order to enhance the overall system efficiency. As a consequence, the cycle duration T is considered as an optimization variable within the OCP (29).

3.3. Characterization of path constraints

Path constraints $\mathbf{h}(\cdot)$ (29c) play an important role for obtaining meaningful flight trajectories. In agreement with both flight envelope constraints and physical limitations of the system, path constraints must be carefully chosen in order to ensure reasonable prediction capability as well as enforce constraints on states and/or control inputs. Furthermore, one should also aim to obtain flight trajectories which allow the aircraft to operate close to some regime, such that classical industrial controllers can perform well.

For this application, path constraints are chosen in agreement with the following observations:

- Crosswind flight should be performed with high angles of attack α , since the lift generated by the aircraft increases as a function α . However, an upper bound of α is required to prevent *stall phenomenon*. Furthermore, the modeled aerodynamic forces and moments presented in Section 1.5 are valid only for attached flows, i. e., low angles of attack [26]. Therefore, one should also bound α in a region where the aerodynamic model accuracy is acceptable.
- As mentioned in Section 2.2, the side slip angle β must be limited to avoid additional drag [11]. Note that, high values of β also involve a non-negligible coupling between the lateral and longitudinal aircraft motions [13].
- The airspeed V_T is bounded in agreement with the flight envelope constraints [22]. It is worth to point out that stall phenomenon may occur at any speed during tethered flights.
- Due to safety issues, the aircraft is constrained to operate above a minimum altitude h_{\min} [23].
- The tether tension f_{t_i} needs to be upper bounded in order to limit mechanical stress on the aircraft structure and tether severance. A lower bound is also required to avoid tether sag effects that mainly arise during the reel-in phase.
- The Euler angles of roll ϕ and pitch θ need to be limited for safety reasons, to avoid possible collisions between tether and airframe, as well as to simplify the control architecture relative to the aircraft attitude [27].
- Tether length l is constrained in agreement with its maximum length.
- Tether speed v_l as well as tether acceleration a_l are bounded in agreement with the winch characteristics.
- Angular velocity relative to the aircraft $\omega^{\mathbf{b}}$ is constrained according to the flight envelope constraints.
- The pumping cycle time T may be bounded, in this case, analyzing the duration of each loop within real flight tests.

Table 6 collects both upper and lower bounds used within this work.

3.4. Characterization of boundary constraints

A generic AWES performs periodic cycles, hence, the boundary constraints $\mathbf{r}(\cdot)$ (29d) should contain the periodicity condition $\mathbf{x}(0) = \mathbf{x}(T)$. Additionally, consistency constraints shown in (28) must be taken into account, too.

It turns out that such combination within an OCP framework produces a Linear Independence Constraint Qualification (LICQ) deficiency caused by redundant constraints [28]. In this case, the orthonormality condition (3) combined with the corresponding periodicity constraint, i. e.,

$$\Xi_c(\mathbf{R}_{\mathbf{nb}}(0)) = \mathbf{R}_{\mathbf{nb}}(0) \cdot \mathbf{R}_{\mathbf{nb}}^T(0) - \mathbf{I}_3 = 0 \quad (34a)$$

Table 6
Path constraints.

Name	Variable	min	max	unit
angle of attack	α	−6.0	9.0	[deg]
angle of side slip	β	−20.0	20.0	[deg]
Airspeed	V_T	13.0	32.0	[m/s]
Altitude	h	100.0	-	[m]
tether tension	f_{t_i}	50.0	1800.0	[N]
roll angle	ϕ	−50.0	50.0	[deg]
pitch angle	θ	−40.0	40.0	[deg]
tether length	l	10.0	700.0	[m]
tether speed	v_l	−15.0	20.0	[m/s]
tether acceleration	a_l	−2.3	2.4	[m/s ²]
Aircraft angular velocity	$\omega^{\mathbf{b}}$	−50.0	50.0	[deg/s]
Aileron deflection	δ_a	−20.0	20.0	[deg]
elevator deflection	δ_e	−30.0	30.0	[deg]
rudder deflection	δ_r	−30.0	30.0	[deg]
servo speed	\mathbf{v}_δ	−2.0	2.0	[rad/s]
trajectory time	T	20.0	70.0	[s]

$$\Xi_p(\mathbf{R}_{\mathbf{nb}}(0), \mathbf{R}_{\mathbf{nb}}(T)) = \mathbf{R}_{\mathbf{nb}}(0) - \mathbf{R}_{\mathbf{nb}}(T) = 0 \quad (34b)$$

deliver LICQ deficiency since nine constraints are enforced (equal to the matrix elements of $\mathbf{R}_{\mathbf{nb}}$) rather than three (the number of degrees of freedom associated to the aircraft attitude).

In order to preserve the LICQ condition, one can enforce respectively three and six matrix elements for the periodicity and orthonormality condition, with specific patterns. According to Refs. [12,17,28], a suitable combination of boundary constraints relative to (34) is given by

$$\tilde{\Xi}_c(\mathbf{R}_{\mathbf{nb}}(0)) = \begin{bmatrix} * & \cdot & \cdot \\ * & * & \cdot \\ * & * & * \end{bmatrix} = 0 \quad (35a)$$

$$\tilde{\Xi}_p(\mathbf{R}_{\mathbf{nb}}(0), \mathbf{R}_{\mathbf{nb}}(T)) = \begin{bmatrix} \cdot & * & * \\ \cdot & \cdot & * \\ \cdot & \cdot & \cdot \end{bmatrix} = 0 \quad (35b)$$

where $*$ denotes the only matrix elements subject to constraints.

Equation (35) are augmented with the additional boundary condition $\tilde{\mathbf{x}}(0) - \tilde{\mathbf{x}}(T) = 0$ where $\tilde{\mathbf{x}}(t)$ is a subset of the state vector $\mathbf{x}(t)$ and equal to

$$\tilde{\mathbf{x}}(t) = [\mathbf{p}^{\mathbf{n}}(t) \quad \mathbf{v}^{\mathbf{b}}(t) \quad \omega^{\mathbf{b}}(t) \quad \delta(t)]^T. \quad (36)$$

Finally, in agreement with the Mayer cost term shown in (32), the energy state E is set equal to zero for $t = 0$.

3.5. Formulation of an OCP for trajectory optimization

In summary, an OCP tailored for AWES to obtain feasible trajectories which maximize the average mechanical power output can be stated as follows:

$$\mathbf{x}(\cdot), \mathbf{z}(\cdot), \mathbf{u}(\cdot), T \int_0^T \left(\|\mathbf{u}(t)\|_{\Sigma_u^{-1}}^2 + \|\dot{\omega}^{\mathbf{b}}(t)\|_{\Sigma_\omega^{-1}}^2 + \sigma_\beta^{-1} \beta^2(t) \right) dt - \frac{E(T)}{T} \quad (37a)$$

$$\mathbf{F}(\dot{\mathbf{x}}(t), \mathbf{x}(t), \mathbf{z}(t), \mathbf{u}(t)) = 0, t \in [0, T] \quad (37b)$$

$$h(t) \geq h_{\min}, t \in [0, T] \quad (37c)$$

$$\alpha_{\min} \leq \alpha(t) \leq \alpha_{\max}, t \in [0, T] \quad (37d) \quad a_{l_{\min}} \leq a_l(t) \leq a_{l_{\max}}, t \in [0, T] \quad (37k)$$

$$V_{T_{\min}} \leq V_T(t) \leq V_{T_{\max}}, t \in [0, T] \quad (37e) \quad \omega_{\mathbf{b}_{\min}} \leq \omega^{\mathbf{b}}(t) \leq \omega_{\mathbf{b}_{\max}}, t \in [0, T] \quad (37l)$$

$$f_{t_{\min}} \leq f_{t_i}(t) \leq f_{t_{\max}}, t \in [0, T] \quad (37f) \quad \delta_{\min} \leq \delta(t) \leq \delta_{\max}, t \in [0, T] \quad (37m)$$

$$\phi_{\min} \leq \phi(t) \leq \phi_{\max}, t \in [0, T] \quad (37g) \quad v_{\delta_{\min}} \leq v_{\delta}(t) \leq v_{\delta_{\max}}, t \in [0, T] \quad (37n)$$

$$\theta_{\min} \leq \theta(t) \leq \theta_{\max}, t \in [0, T] \quad (37h) \quad \tilde{\mathbf{x}}(0) - \tilde{\mathbf{x}}(T) = 0, \quad (37o)$$

$$l_{\min} \leq l(t) \leq l_{\max}, t \in [0, T] \quad (37i) \quad \tilde{\mathbf{E}}_p(\mathbf{R}_{\mathbf{nb}}(0), \mathbf{R}_{\mathbf{nb}}(T)) = 0, \quad (37p)$$

$$v_{l_{\min}} \leq v_l(t) \leq v_{l_{\max}}, t \in [0, T] \quad (37j) \quad c(\mathbf{x}(0)) = 0, \dot{c}(\mathbf{x}(0)) = 0, \quad (37q)$$

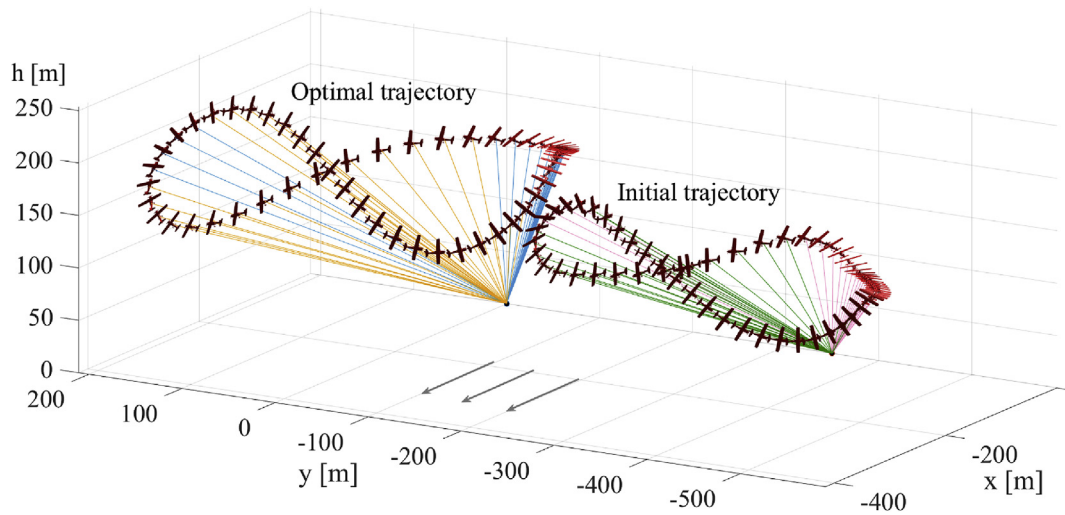


Fig. 6. Comparison in 3D between optimal open-loop trajectory (left) and simulated closed-loop trajectory (right) used as initial guess with average wind speed at operating altitude $w(h) \approx 10\text{m/s}$. In the open(closed)-loop solution the reel-in phase is denoted with blue(pink) tether, whereas the orange(green) tether corresponds to the reel-out phase. The main reel-in phase arises in the right corner (picture view), though, a further reel-in phase occurs in the left corner to prevent loss of airspeed of the airborne component. (For interpretation of the references to colour in this figure legend, the reader is referred to the Web version of this article.)

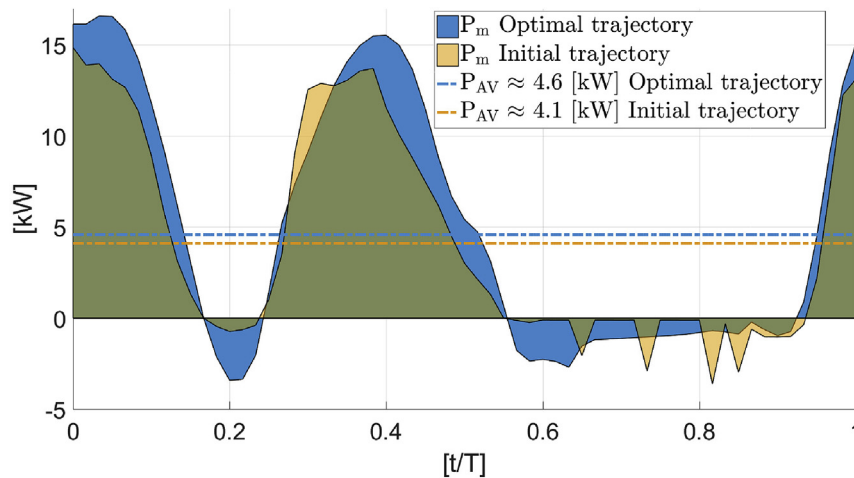


Fig. 7. Mechanical power P_m comparison between optimal open-loop trajectory and closed-loop simulation with corresponding average power output P_{AV} , with normalized time scale. The tether speed v_l and tether tension f_t , produce a certain amount of mechanical power P_m that is subsequently converted to electrical power P_e by the generator. Under optimal conditions, the expected average mechanical power output P_{AV} is roughly 4.6 kW, whereas it is expected that the current control system implemented by Ampyx Power B.V. causes a loss of performance $\approx 10\%$ w.r.t. the optimal scenario.

$$\bar{\mathbf{m}}_c(\mathbf{R}_{nb}(0)) = 0, E(0) = 0. \quad (37r)$$

where (37b) denotes the mathematical model described as an index-1 DAE. The inequalities from (37c) to (37n) correspond to the path constraints described in Section 2.3. Boundary constraints are characterized by the periodicity conditions (37°) and (37p). Finally, Equation (37q) and (37r) ensure that the system dynamics evolve within the prescribed manifold.

3.6. Algorithm implementation

Within this work, the OCPs are computed using OPENAWE [29], an open-source tool for the Matlab/Octave environment. OPENAWE is implemented using object oriented programming and it contains a library for modeling components of a typical AWES such as aircraft, winch, and tether. OPENAWE is built upon an open-source optimal control library named OPENOCL [30] and based on CASADI [31].

In short, the continuous-time optimization problem is

discretized and formulated as a NLP automatically by OPENOCL using direct collocation techniques [32]. For this application, a Radau scheme that uses $k = 3$ collocation points is chosen. The resulting NLP is subsequently solved by IPOPT [33] with linear solver MA27 [34].

In Ref. [35] it is possible to find a simplified, non-confidential version of the proposed work based on the case study.

3.7. OCP validation and optimal control strategy

Flight trajectories that are carried out via an optimal control approach are based on strong assumptions, such as that the mathematical formulation which describes the system dynamics of the real plant is fully free from model mismatch and parametric uncertainty. Additionally, one implicitly assumes that the plant operates in a disturbance-free scenario. Hence, if these assumptions were true, the real plant can operate in *open-loop*, i. e., no feedback controls are required. However, the mathematical representation of an AWES is subject to many uncertainties and it relies on several model assumptions. Further, the system operates in a

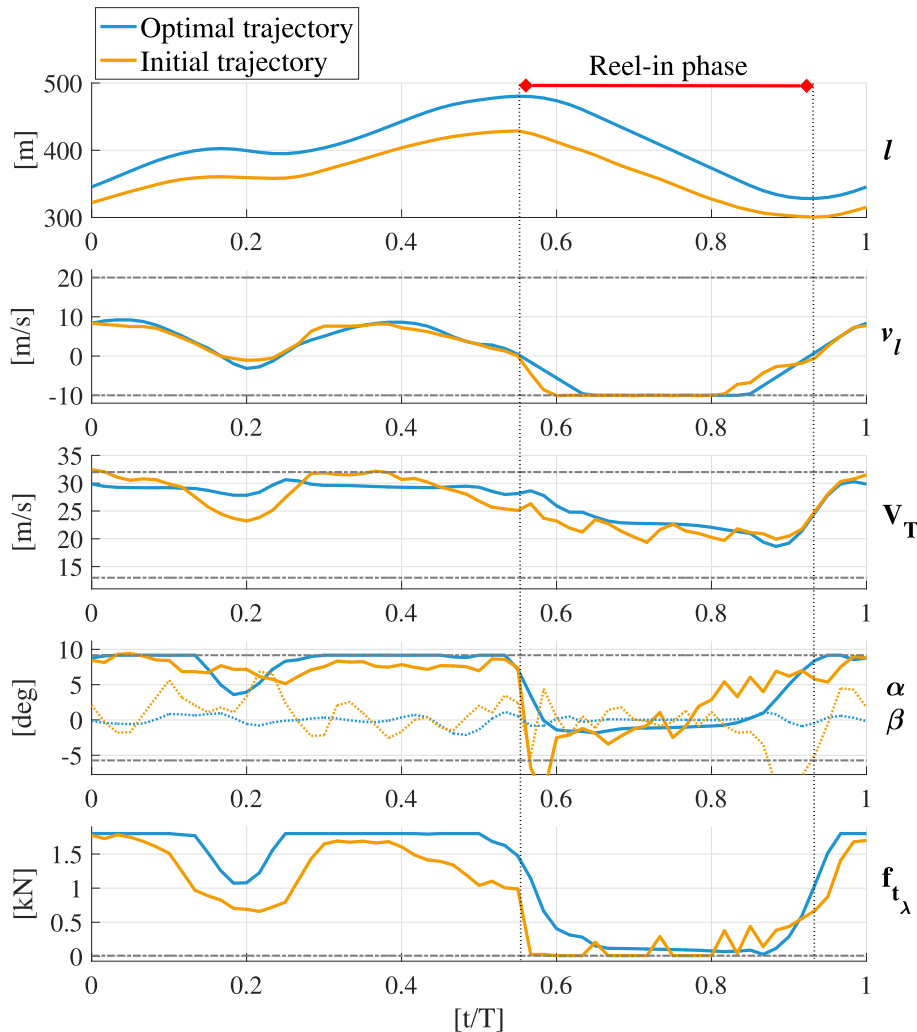


Fig. 8. Comparison between optimal open-loop (blue) and closed-loop simulation (orange) used as initial guess. From the top it is shown in normalized time scale the tether length l , tether speed v_l , airspeed V_T , angle of attack α , angle of side slip β (dot lines) and tether tension f_{t_λ} . Path constraints are shown in dash dot grey line. In both cases a second reel-in phase occurs in order to prevent the loss of airspeed of the aircraft. The pumping cycle time is $T \approx 50$ s and $T \approx 43$ s for the optimal and initial trajectory, respectively. Finally, as far as it regards the angle of side slip β , on the one hand its value is kept close to zero (as required) along the entire optimal trajectory. On the other hand, the control system designed by Ampyx Power B.V. is capable to bound β under realistic atmospheric conditions. (For interpretation of the references to colour in this figure legend, the reader is referred to the Web version of this article.)

gusty environment. As a consequence, the model prediction deviates from the actual plant behavior.

In order to deal with such *model-plant mismatch* issues, it is common practice to design ad-hoc feedback control systems with specific margins of robustness. Therefore, in a real environment the plant operates in *closed-loop*, though, from classical control theory it is well known that robust feedback laws involve a degradation of the overall system performance. Additionally, industrial control systems are often tuned via heuristic techniques which may lead to further performance losses.

Ideally, for validation purposes one should compare the OCP outcome with experimental data sets where the reference input tracking is a computed optimal flight trajectory. Unfortunately, only experimental data sets carried out with flight trajectories tuned via heuristic techniques are available. In this case, one can still validate the optimal outcomes by initializing the OCP (37) with a simulated closed-loop solution obtained by the actual FCC. Subsequently, the system performance can be compared in terms of average power output. Validation results are then satisfactory if the deviation of the average power output P_{AV} between the open and closed-loop trajectory obtained in a simulation environment is roughly equal to the corresponding deviation obtained within a real environment.

In agreement with the considerations mentioned above, let us initialize the OCP (37) with initial position \mathbf{p}^n , translational velocity \mathbf{v}^n (both in NED frame) and DCM \mathbf{R}_{nb} obtained via the highly accurate simulator designed by Ampyx Power B.V [5]. The closed-loop simulation is carried out under realistic atmospheric conditions and using the actual control system embedded in the FCC.

In Figs. 6–8 the initial guess (closed-loop simulation) is compared with the corresponding optimal open-loop solution. The OCP converges to a wider trajectory with a slightly higher elevation angle compared to the closed-loop simulation retrieved by tracking a flight trajectory heuristically tuned. As expected, an optimal control strategy suggests to perform crosswind flights with high angle of attack α and high airspeed V_T . As a result, the lift generated by the aircraft causes a high tension which is used to unroll the tether with speed v_r . During the reel-in phase, the angle of attack decreases simultaneously with the airspeed, while the tether tension drops and the aircraft climbs up to a predefined altitude h .

Simultaneously, the winch rolls up the tether with low tension (hence low power consumption) and maximum tether speed. Note that a further reel-in phase occurs in both cases at the left corner (Fig. 6 picture view). After the power production phase, the aircraft must regain altitude, but the kinetic energy is not sufficient to restore the desired altitude, due to dissipative effects coming from aerodynamic drag of both tether and aircraft. As a consequence, during the climbing phase the aircraft slows down and the winch is prone to perform an additional reel-in phase to prevent loss of airspeed of the aircraft, and eventually to avoid slack phenomena in the tether. Such behavior has also been experienced within real crosswind flight tests as described in Ref. [27].

In an optimal scenario the expected average power output P_{AV} is roughly 4.6 kW, whereas in a sub-optimal scenario characterized by a cascade control architecture described in Ref. [27], with reference input tracking a flight trajectory tuned with heuristic techniques, the performance is reduced by $\approx 10\%$ w.r.t. the optimal scenario. Such loss of performance might be attributed primarily to the tracker controllers relative to the tether tension and the angle of attack.

The tension controller is based on an indirect control of the tether tension by means of the winch speed, and results shown in Fig. 8 suggest there might be margin of improvement in terms of system efficiency by either performing a better tuning of the control gains, or by directly changing the control input used to track the tether tension.

As far as it regards the angle of attack, it turns out that the designing of a controller which is able to keep the angle of attack constant during crosswind flights is rather difficult. As a result, the lift generated during the power generation phase is not uniform and with a minor magnitude w.r.t. the optimal scenario.

Once the gap between the optimal open-loop trajectory and the closed-loop simulation performed with the actual set-up is known, the optimal solution is measured against real crosswind flights. For the purpose of validation, the mechanical average power output P_{AV} is taken into account. The experimental data set is retrieved from Ref. [27] and they are shown in Fig. 9 compared to optimal values obtained via the OCP (37).

For this application, results show that the actual system

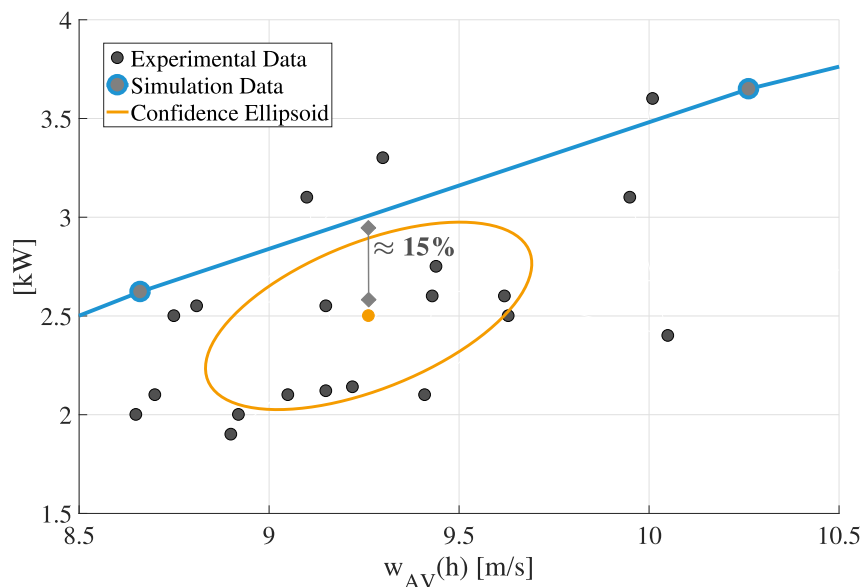


Fig. 9. Optimal average power output P_{AV} (grey dots) with corresponding interpolation (blue line) compared against an experimental data set (black dots). (For interpretation of the references to colour in this figure legend, the reader is referred to the Web version of this article.)

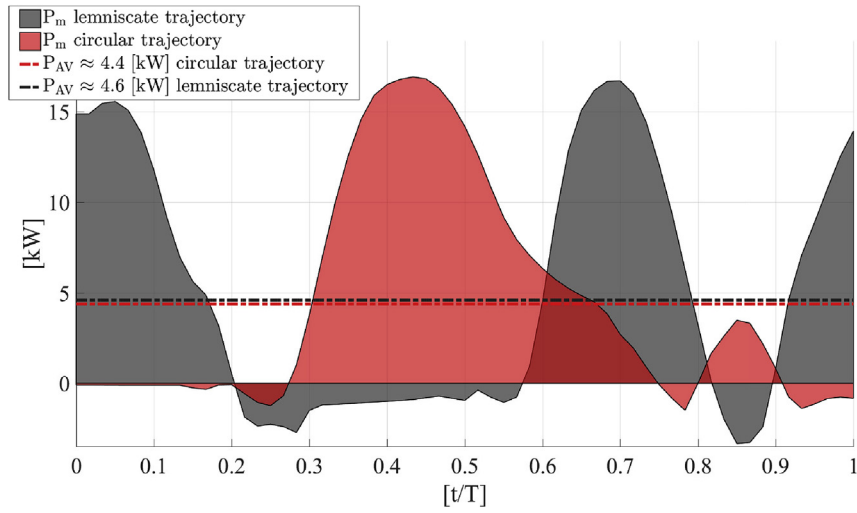


Fig. 10. Average power outputs comparison with normalized time between lemniscate and circular trajectory.

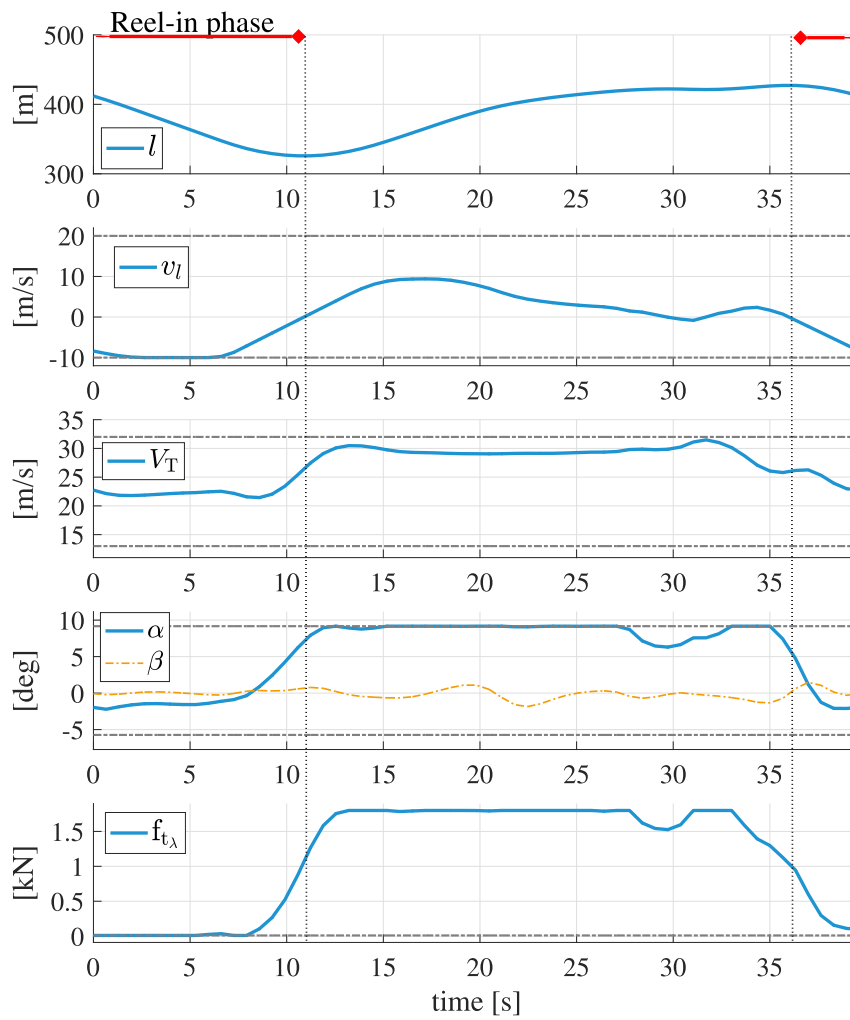


Fig. 11. Optimal solution relative to tether length l , tether speed v_l , airspeed V_T , angle of attack α , angle of side slip β and tether tension f_t , for a circular flight trajectory. Path constraints are shown in dash dot grey line.

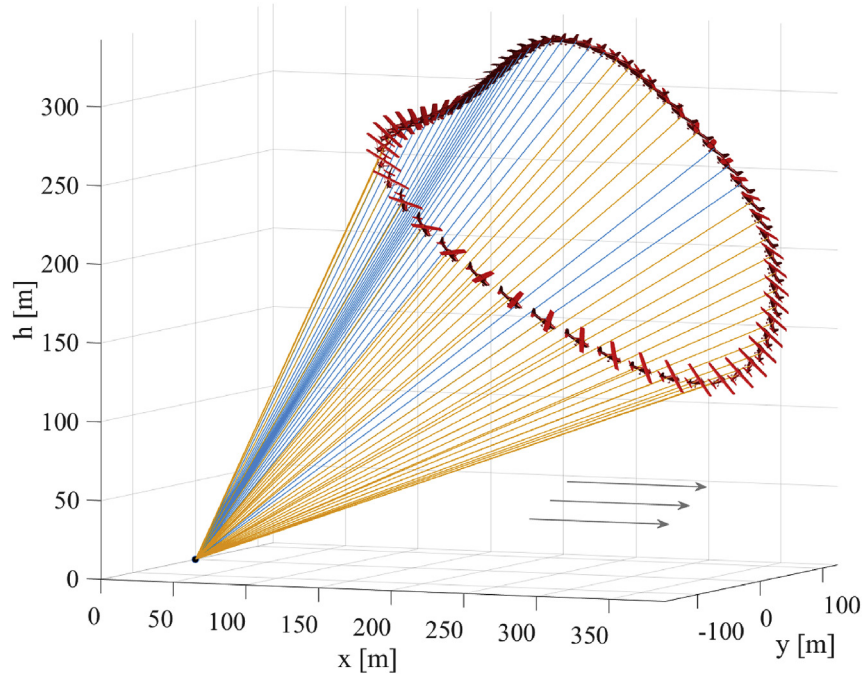


Fig. 12. Optimal trajectory for a rigid wing pumping mode AWES in 3D (circular pattern). The blue tether corresponds to the reel-in (power consumption) phase, while the orange tether denotes the reel-out (power production) phase. (For interpretation of the references to colour in this figure legend, the reader is referred to the Web version of this article.)

performance is reduced by roughly 15% w.r.t. to the predicted optimal behavior, where $\approx 10\%$ are associated to the controllers performance, whereas the remaining 5% are caused by communication latencies between the aircraft and the ground station as pointed out in Ref. [27], and turbulence. Further, various model-plant mismatches act on the overall system performance, e. g., due to the simplification of the wind shear, inaccuracy in the aerodynamic properties as well as tether dynamics approximation with corresponding drag assumed within this work.

4. System performance analysis

In this section, several scenarios are analyzed in terms of trajectory shape, control strategy, average power output, and for different wind condition. Finally, the power curve of the case study is carried out together with its harvesting factor.

4.1. Lemniscate versus circular optimal trajectory

In the AWE field, two common trajectory typologies are considered: lemniscate and circular trajectory. On the one hand, a circular trajectory is often preferred in practice for its simplicity, though, the winch must be equipped with a swivel mechanism in order to avoid tether winding issues. On the other hand, a lemniscate trajectory avoids swivel mechanisms, though, the aircraft might be subject to high angular accelerations [36].

Since a common goal for an AWES is the maximization of the average power output P_{AV} , one can assess which flight trajectory delivers the highest P_{AV} under equal boundary conditions. For this purpose, we solve the OCP in (37) using a circular trajectory as initial guess, and compare it with respect to the optimal lemniscate trajectory obtained in Section 2.7. Note that, in this case an *homotopy strategy* was used to compute a feasible initial guess [36].

The obtained optimal circular trajectory for the case study is depicted in Fig. 12. Despite the difference in terms of topology, both trajectories exhibit the same control strategy that is described in

Section 2.7. Furthermore, in both cases the average power output P_{AV} is close to 4.5 kW, as shown in Fig. 10. Therefore, under the assumption of equal boundary conditions, a rigid wing pumping mode AWES harvests the same amount of energy over the time T regardless of the topology of the flight trajectory, in other words, P_{AV} is not sensitive to the trajectory topology (see Fig. 11).

Nevertheless, AWES need to be arranged in wind farms, i. e. a set of AWES installed at the same location with a specific layout, in order to generate a noticeable amount of energy. As shown in Fig. 13, for conventional wind farms it is common practice to introduce spacing between wind turbines equal to $14 l_B$ in the wind prevalent direction and $8 l_B$ in the transverse direction with l_B the blade length, so that the *wake effects* are minimized [37].

A standardized layout for AWE farms is object of ongoing research, though, it is expected that wake losses are quite limited in

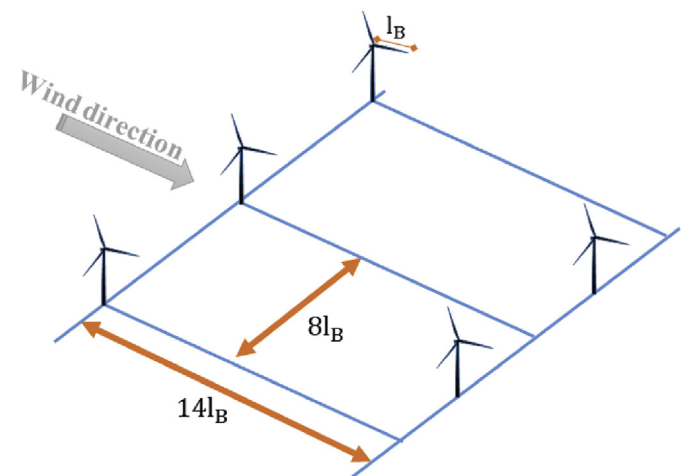


Fig. 13. Layout of conventional wind farms [38]. The variable l_B denotes the blade length.

comparison to conventional wind turbines. As a consequence, the spacing between AWES can be significantly reduced so that the surface power density (MW/km^2) is enhanced. Additionally, one can compare the flight trajectories previously obtained to assess which topology may require less surface. It turns out that despite both trajectories theoretically produce the same amount of power, the circular trajectory is less wide than the lemniscate trajectory (see Fig. 14). As a consequence, in an AWE farm, circular trajectories can deliver a higher surface power density compared to lemniscate trajectories.

Exemplary, let us consider the layout proposed in Ref. [39] with a facility density of $1.2/l_{\text{max}}^2$ where l_{max} is the maximum tether length. The layout implicitly assumes that the aircraft trajectories do not interfere each other with additional safety margin. Results show that for this specific set-up, circular trajectories can reduce up to $\approx 40\%$ of area required compared to lemniscate trajectories, see Fig. 15.

4.2. Power curve and flight trajectories for different wind speeds

Reliable tools capable of computing performance analyses of an AWES prior to real experiments are crucial for viability assessments for scaling-up purposes. Similarly to conventional wind turbines, AWES performance can be evaluated by analyzing their corresponding power curves, i. e., the net power produced along a range of wind speeds. However, in contrast to other wind energy conversion systems, the net electrical power output of an pumping mode AWES refers to the average power that the system can generate over the whole pumping cycle under optimal conditions [40].

In principle, power curves can be very costly to compute for a given AWES, since numerous variables need to be taken into account simultaneously, e. g.,

- maximum sustainable tension within the reel-out (power production) phase;
- power consumption during the reel-in phase;
- duration of reel-in and reel-out phase per loop;
- aerodynamic characteristics such as lift and drag curve of the airborne component;

- elevation angle and tether length.

Within an optimization framework, the power curve can be systematically obtained by solving a sequence of OCPs (37) for a range of wind speeds. The OCPs take into account equal wind shear, though, with different wind speed magnitudes that are varied by the wind speed measured at the anemometer height w_{h_a} (see (1)). Once the first OCP is solved, the subsequent OCP can be initialized with the previous solution and for a different value of w_{h_a} .

In Fig. 16, an example of trajectories associated to the cases of low, medium and high wind conditions is shown. During low wind conditions, the plant operates with a high elevation angle, whereas the aircraft flies close to the winch so as to reduce the drag associated to the tether. By increasing the wind speed, the elevation angle decreases and the aircraft performs crosswind flights adopting a control strategy described in Section 2.7. With a further increment of the wind speed, the plant is prone to operate newly with a high elevation angle, though far from the winch in order to limit the tension in the tether, whereas the trajectory size increases, as well as the reel-in phase.

Fig. 17 shows the power curve relative to the case study, evaluated within a range of w_{h_a} from 0 m/s to 20 m/s with a step size of 1 m/s and interpolated subsequently. Note that the x-axis corresponds to the average wind speed at operating altitude w_{AV} . The power curve is divided into four parts. Between zero and the cut-in wind speed, $w(h) \approx 4$ m/s, the aircraft is kept aloft using optimal holding patterns via a reversed pumping strategy [22]. In this case, the net power output produced along the flight trajectory is negative due to low wind conditions. From the cut-in wind speed onwards, power production reaches its maximum value of ≈ 9 kW for $w(h) \approx 22$ m/s. In the third part, system performance slightly decreases due to a higher investment in terms of both time and energy required during the reel-in phase. Beyond the cut-out speed $w(h) \approx 25$ m/s, it is assumed that the plant does not operate for safety reasons, hence, no power is produced.

The system performance is further assessed by means of the Power Harvesting Factor ξ , which is defined for a specific average wind speed $w_{\text{AV}}(h)$ at operating altitude h as

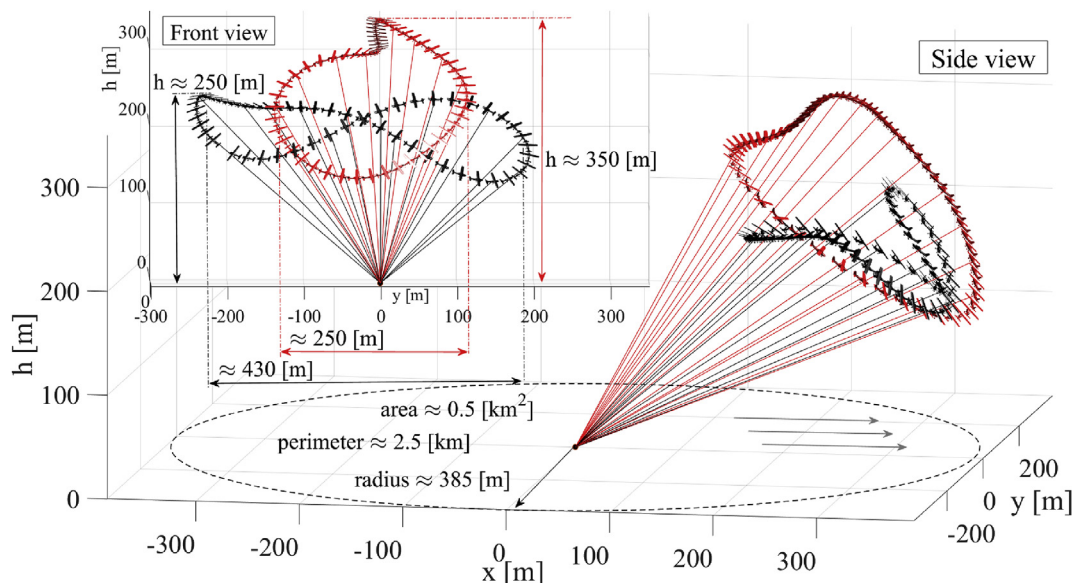


Fig. 14. Size comparison between lemniscate and circular trajectory under equal boundary conditions.

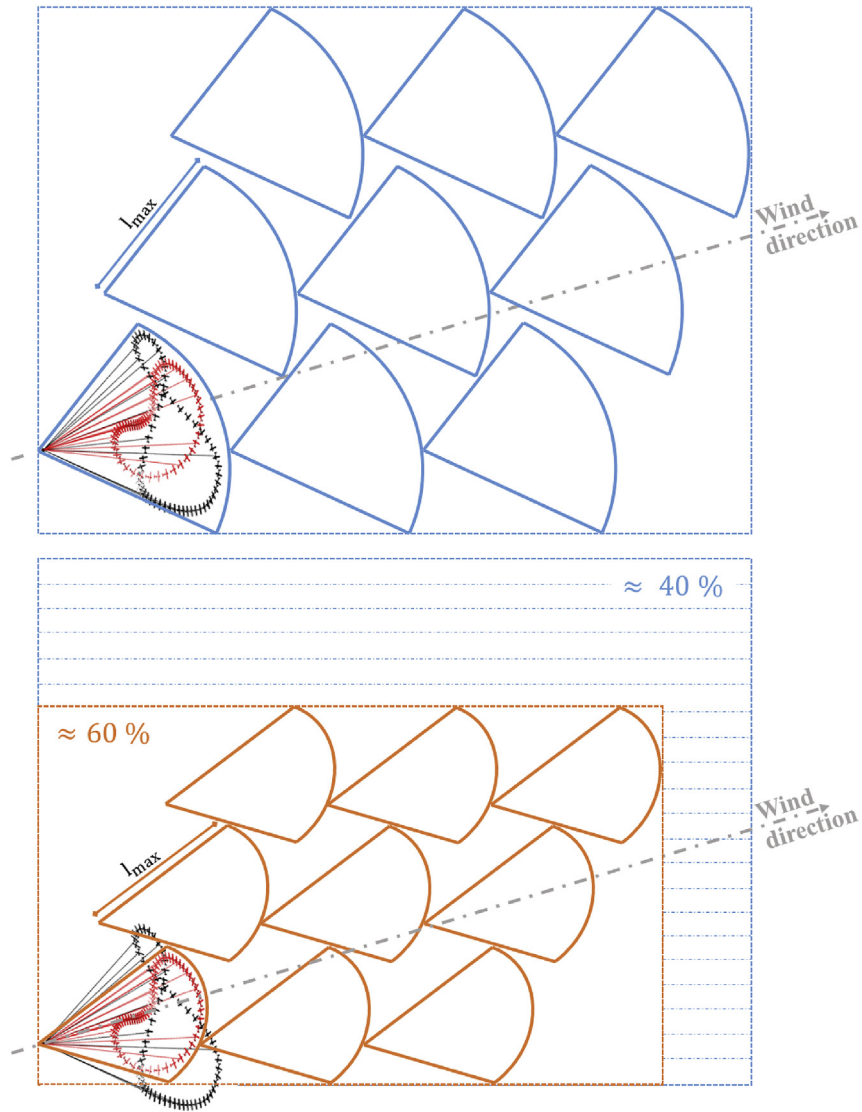


Fig. 15. AWE farm layout with facility density of $1.2/l_{max}^2$ for a given wind direction proposed in Ref. [39]. The variable l_{max} denotes the maximum tether.

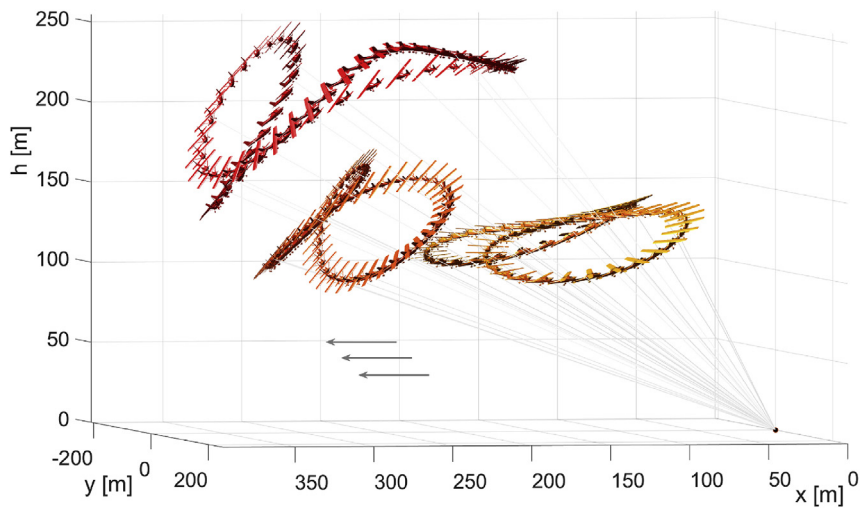


Fig. 16. Example of trajectories associated to the cases of low, medium and high wind conditions. The grey arrows denote the wind direction.

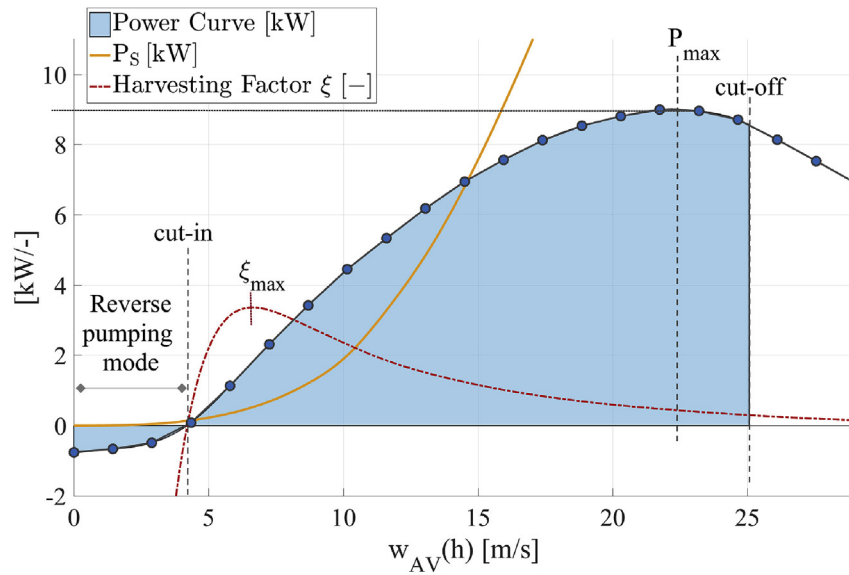


Fig. 17. System performance expressed in power curve. In the y-axis, optimal average mechanical power P_{AV} (blue dot line), theoretical power produced by a wing of area A (orange line), and power harvesting factor ξ (dash-dot red line) versus average wind speed at operating altitude $w(h)$ (x-axis). (For interpretation of the references to colour in this figure legend, the reader is referred to the Web version of this article.)

$$\xi = \frac{P_{AV}}{P_S} \quad (38)$$

where P_S denotes the wind power that flows through the cross sectional area of size equal to the aircraft wing area S , i. e.,

$$P_S = \frac{1}{2} \rho S w_{AV}^3(h). \quad (39)$$

Nowadays, conventional wind turbines have a Power Harvesting Factor of approximately 5.5 [41]. For the case study, the maximum Power Harvesting Factor ξ_{max} is ≈ 3.5 and it occurs at $w_{AV}(h) \approx 6.5$ m/s, as also depicted in Fig. 16. Such a low value is not surprising since the plant considered within this work is used as a case-study for testing and verification purposes only.

5. Conclusions

This work presented an optimal control-based performance assessment of a rigid wing pumping mode AWES. Through solution of a tailored OCP, wherein the AWES is represented by an index-1 DAE, flight trajectories for varying operation conditions and trajectory topologies have been obtained. For formulation and solution of the OCP, the open-source toolbox *OPENAWES* has been used, of which a non-confidential version has been released [29].

The system characteristics as well as the path constraints were defined in agreement with an existing AWES, which is the 2nd prototype of Ampyx Power B.V [5]. For validation of the results obtained by the OCP, the results have been compared to a set of experimental data in terms of mechanical average power output and the discrepancy between the optimal open-loop solution of the OCP and a simulated closed-loop solution carried out using the actual FCC designed by Ampyx Power B.V. has been quantified. It turns out that non-optimal flight trajectories combined with a cascade control architecture characterized by well tuned industrial controllers can achieve performances close to the optimal scenario. For this specific application the performance losses were $\approx 10\%$ (under the assumption of no communication latencies) caused by a non optimal tracking of both tether tension and angle of attack.

Afterwards, a comparison of using a lemniscate trajectory and a circular trajectory for operation of an AWES under equal boundary conditions has been carried out. The comparison shows that the amount of power per loop produced by the AWES is equal for both trajectories and that the performance of the AWES therefore is independent of the chosen trajectory topology. However, due to a smaller width of the flight pattern, use of circular trajectories might possibly deliver a higher surface power density compared to lemniscate trajectories, which is especially interesting for design and operation of AWES wind farms.

Finally, a sequence of OCPs has been solved for a range of wind speeds to obtain the power curve and harvesting factor for the AWES utilized within this case study and the corresponding optimal flight trajectories. It shows that in low wind conditions, the optimization tool suggests to perform holding patterns with minimum allowable altitude and close to the ground station to minimize the tether drag and consequently the power losses. For high wind speeds on the other hand, it is advisable to increase both tether length and elevation angle to limit the tension on the airframe during the power generation phase.

Future works

Future works will aim toward the performance assessment of a rigid wing pumping mode AWES for different set of physical characteristics such as mass, inertia and aerodynamic properties.

References

- [1] Archer CL. An introduction to meteorology for Airborne Wind Energy. In: Airborne Wind Energy. Springer; 2013. p. 81–94. https://doi.org/10.1007/978-3-642-39965-7_5.
- [2] Diehl M, Schmehl R, Ahrens U. Airborne Wind Energy. Green energy and technology. Springer Berlin Heidelberg; 2014. <https://doi.org/10.1007/978-3-642-39965-7>.
- [3] Loyd ML. Crosswind kite power (for large-scale wind power production). *J Energy* 1980;4(3):106–11.
- [4] Makani, <https://x.company/makani/> (2017).
- [5] Ampyx power: Airborne Wind Energy. 2018. <https://www.ampyxpower.com>.
- [6] Kps, <http://www.kps.energy/> (2018).
- [7] Twingtec. Wind energy 2.0. 2017. <http://twingtec.ch/>.
- [8] kitemill, <http://www.kitemill.com/> (2017).

- [9] e-kite, <http://www.e-kite.com/> (2017).
- [10] Horn G, Gros S, Diehl M. Numerical trajectory optimization for Airborne Wind Energy systems described by high fidelity aircraft models. In: Airborne Wind Energy. Springer; 2013. p. 205–18. https://doi.org/10.1007/978-3-642-39965-7_11.
- [11] Mulder J, Van Staveren W, van der Vaart J. Flight dynamics (lecture notes). TU Delft; 2000.
- [12] Gros S, Diehl M. Modeling of Airborne Wind Energy systems in natural coordinates. In: Airborne Wind Energy. Springer; 2013. p. 181–203. https://doi.org/10.1007/978-3-642-39965-7_10.
- [13] Stevens BL, Lewis FL, Johnson EN. Aircraft control and simulation: dynamics, controls design, and autonomous systems. Wiley; 2015. <https://doi.org/10.1002/9781119174882>.
- [14] Williams P, Trivailo P. Dynamics of circularly towed aerial cable systems, part i: optimal configurations and their stability. J Guid Contr Dynam 2007;30(3): 753–65. <https://doi.org/10.2514/1.20433>.
- [15] Williams P, Trivailo P. Dynamics of circularly towed aerial cable systems, part 2: transitional flight and deployment control. J Guid Contr Dynam 2007;30(3): 766–79. <https://doi.org/10.2514/1.20434>.
- [16] Williams P, Lansdorp B, Ockels W. Modeling and control of a kite on a variable length flexible inelastic tether. In: Guidance, navigation and control conference. AIAA; 2007. <https://doi.org/10.2514/6.2007-6705>.
- [17] Zanon M, Gros S, Diehl M. Model predictive control of rigid-airfoil Airborne Wind Energy systems. In: Airborne Wind Energy. Springer; 2013. p. 219–33. https://doi.org/10.1007/978-3-642-39965-7_12.
- [18] Zanon M, Gros S, Andersson J, Diehl M. Airborne Wind Energy based on dual airfoils. IEEE Trans Control Syst Technol 2013;21(4):1215–22. <https://doi.org/10.1109/TCST.2013.2257781>.
- [19] Argatov I, Rautakorpi P, Silvennoinen R. Estimation of the mechanical energy output of the kite wind generator. Renew Energy 2009;34(6):1525–32. <https://doi.org/10.1016/j.renene.2008.11.001>.
- [20] Houska B, Diehl M. Optimal control for power generating kites. In: European control conference (ECC). IEEE; 2007. p. 3560–7.
- [21] Argatov I, Silvennoinen R. Efficiency of traction power conversion based on crosswind motion. In: Airborne Wind Energy. Springer; 2013. p. 65–79. https://doi.org/10.1007/978-3-642-39965-7_4.
- [22] Licitra G, Sieberling S, Engelen S, Williams P, Ruiterkamp R, Diehl M. Optimal control for minimizing power consumption during holding patterns for Airborne Wind Energy pumping system. In: European control conference (ECC). IEEE; 2016. p. 1574–9. <https://doi.org/10.1109/ECC.2016.7810515>.
- [23] Licitra G, Koenemann J, Horn G, Williams P, Ruiterkamp R, Diehl M. Viability assessment of a rigid wing Airborne Wind Energy pumping system. In: 21st international conference on process control (PC). IEEE; 2017. p. 452–8. <https://doi.org/10.1109/PC.2017.7976256>.
- [24] Ascher UM, Petzold LR. Computer methods for ordinary differential equations and differential-algebraic equations, vol. 61. SIAM; 1998. <https://doi.org/10.1137/1.9781611971392>.
- [25] Diehl M, Gros S. Numerical optimal control. University of Freiburg; 2017. <https://www.syscop.de/files/2017ss/NOC/script/book-NOCSE.pdf>.
- [26] Etkin B. Dynamics of atmospheric flight. Wiley; 1972.
- [27] Ruiterkamp R, Sieberling S. Description and preliminary test results of a six degrees of freedom rigid wing pumping system. In: Airborne Wind Energy. Springer; 2013. p. 443–58. https://doi.org/10.1007/978-3-642-39965-7_26.
- [28] S. Gros, Numerical optimal control with differential algebraic equations, <https://www.syscop.de/teaching/ws2015/nocdae> (Feb 2016).
- [29] Koenemann J. Openawe – open Airborne Wind Energy. 2017. <https://openawe.github.io/>.
- [30] Koenemann J. Openocl – open optimal control library. 2017. <http://www.openocl.org/>.
- [31] Andersson Joel AE, Gillis Joris, Horn Greg, Rawlings James B, Diehl Moritz. CasADi – a software framework for nonlinear optimization and optimal control. Math Program. Comput. 2018 in press.
- [32] Biegler LT. Nonlinear programming: concepts, algorithms, and applications to chemical processes, vol. 10. Siam; 2010. <https://doi.org/10.1137/1.9780898719383>.
- [33] Wächter A, Biegler LT. On the implementation of an interior-point filter line-search algorithm for large-scale nonlinear programming. Math Program 2006;106(1):25–57. <https://doi.org/10.1007/s10107-004-0559-y>.
- [34] HSL. A collection of fortran codes for large scale scientific computation. 2017. <http://www.hsl.rl.ac.uk/>.
- [35] Koenemann J, Licitra G. Flight trajectories optimization of rigid wing pumping mode awes. 2017. <https://github.com/openawe/openawe>.
- [36] Gros S, Zanon M, Diehl M. A relaxation strategy for the optimization of Airborne Wind Energy systems. In: European control conference (ECC). IEEE; 2013. p. 1011–6.
- [37] Samorani M. The wind farm layout optimization problem. Springer; 2013. https://doi.org/10.1007/978-3-642-41080-2_2.
- [38] Fagiano L. Control of tethered airfoils for high altitude wind energy generation. Ph.D. thesis. Politecnico di Torino; 2009.
- [39] Kruijff M, Ruiterkamp R. A roadmap towards Airborne Wind Energy in the utility sector. In: Airborne Wind Energy. Green energy and technology. Singapore: Springer; 2018. https://doi.org/10.1007/978-981-10-1947-0_26.
- [40] Heilmann J, Houle C. Economics of pumping kite generators. In: Airborne Wind Energy. Springer; 2013. p. 271–84. https://doi.org/10.1007/978-3-642-39965-7_15.
- [41] Diehl M. Airborne Wind Energy: basic concepts and physical foundations. In: Airborne Wind Energy. Springer; 2013. p. 3–22. https://doi.org/10.1007/978-3-642-39965-7_1.
- [42] Masters GM. Renewable and efficient electric power systems. John Wiley & Sons; 2013. <https://doi.org/10.1002/0471668826>.